RSC Advances

PAPER

View Article Online
View Journal | View Issue

Cite this: *RSC Adv.*, 2018, **8**, 5180

Novel magnetic g-C_3N_4/α-Fe_2O_3/Fe_3O_4 composite for the very effective visible-light-Fenton degradation of Orange II

Zhuliang Wang,[ab] Yiping Fan,[a] Rong Wu,[a] Yaoxing Huo,[a] Hao Wu,[*ab] Fang Wang[ab] and Xiaohong Xu[*ab]

A novel magnetic heterogeneous g-C_3N_4/α-Fe_2O_3/Fe_3O_4 catalyst was successfully synthesized through a simple hydrothermal method. The structure, morphology, and optical properties of the catalyst were characterized. The photocatalytic activity of the heterogeneous g-C_3N_4/α-Fe_2O_3/Fe_3O_4 catalyst for the photo-Fenton degradation of Orange II in the presence of H_2O_2 irradiated with visible light ($\lambda > 420$ nm) at neutral pH was evaluated. The g-C_3N_4/α-Fe_2O_3/Fe_3O_4 photocatalyst was found to be an excellent catalyst for the degradation of Orange II and offers great advantages over the traditional Fenton system (Fe(II/III)/H_2O_2). The results indicated that successfully combining monodispersed Fe_3O_4 nanoparticles and g-C_3N_4/α-Fe_2O_3 enhanced light harvesting, retarded photogenerated electron–hole recombination, and significantly enhanced the photocatalytic activity of the system. The g-C_3N_4/α-Fe_2O_3/Fe_3O_4 (30%) sample gave the highest degradation rate constant, 0.091 min^{-1}, which was almost 4.01 times higher than the degradation rate constant for α-Fe_2O_3 and 2.65 times higher than the degradation rate constant for g-C_3N_4/α-Fe_2O_3 under the same conditions. A reasonable mechanism for catalysis by the g-C_3N_4/α-Fe_2O_3/Fe_3O_4 composite was developed. The g-C_3N_4/α-Fe_2O_3/Fe_3O_4 composite was found to be stable and recyclable, meaning it has great potential for use as a photo-Fenton catalyst for effectively degrading organic pollutants in wastewater.

Received 13th December 2017
Accepted 20th January 2018

DOI: 10.1039/c7ra13291c

rsc.li/rsc-advances

1. Introduction

Increasing amounts of synthetic organic dye pollutants are being released into the environment after synthetic dyes have been used in the textile, leather, pharmaceutical, food, and other industries.[1] Advanced oxidation processes including ozonation, Fenton reactions, photo-Fenton reactions, photocatalysis, ultrasonication, and other processes can potentially be used to degrade recalcitrant organic contaminants because total mineralization is more likely to be achieved using advanced oxidation processes than using classical wastewater treatment processes.[2–7] The Fenton reaction, an advanced oxidation process, involves producing radicals using homogeneous Fe(II/III) and H_2O_2. The Fenton reaction has been shown to be an effective treatment for wastewater produced by various industries because it is fast, simple to perform, and does not produce toxic products[8,9] However, there are some drawbacks to homogeneous processes such as the Fenton reaction in that sludge is generated, the pH must be adjusted before and after the reaction, and the catalyst is lost in the effluent. These drawbacks limit the applications of the Fenton reaction.[10] Using a solid catalyst in a "heterogeneous Fenton oxidation reaction" may solve these problems.[11,12]

Hematite (α-Fe_2O_3), a common semiconductor with a narrow band gap of 1.9–2.1 eV, has been used as a heterogeneous photo-Fenton catalyst. α-Fe_2O_3 is easy and cheap to produce, nontoxic, and can be used over a wide pH range.[13] The photocatalytic degradation efficiency achieved using α-Fe_2O_3 can be markedly increased by coupling the α-Fe_2O_3 with other oxides or semiconductors.[14–20] Graphitic carbon nitride (g-C_3N_4), which has been studied in recent years, is a typical metal-free polymeric semiconductor that is very chemically stable and environmentally benign, and it has been found to have a band gap of 2.7 eV, making it suitable for absorbing visible light. g-C_3N_4 is therefore a promising candidate for coupling with α-Fe_2O_3 to form a heterogeneous photo-Fenton catalyst. Many attempts have been made to fabricate α-Fe_2O_3/g-C_3N_4 composites for photodegrading organic dyes using visible light.[21,22] However, the g-C_3N_4/α-Fe_2O_3 heterogeneous catalyst is not appropriate for practical use because it is difficult to remove from suspension and reuse. Magnetically separable photocatalysts have

[a]*School of Chemistry and Materials Science of Shanxi Normal University, Key Laboratory of Magnetic Molecules and Magnetic Information Materials of Ministry of Education, Linfen, 041004, China. E-mail: xuxh@sxnu.edu.cn; wuhao@sxnu.edu.cn*

[b]*Research Institute of Materials Science of Shanxi Normal University, Collaborative Innovation Center for Shanxi Advanced Permanent Magnetic Materials and Techonology, Linfen, 041004, China*

attracted considerable interest because they can be removed from suspensions easily.

Many magnetic materials are available (*e.g.*, Fe_3O_4, γ-Fe_2O_3, and MFe_2O_4, where M is Ba^{2+}, Co^{2+}, Mg^{2+}, Mn^{2+}, Ni^{2+}, or Zn^{2+}). Magnetite (Fe_3O_4) is one of the most popular materials for producing magnetically recoverable catalysts because it is cheap, has a desirable degree of magnetism, and is nontoxic.[23] However, Fe_3O_4 is very conductive, so it can transfer photogenerated electrons rapidly, improving charge carrier separation efficiency.[24] It has recently been found that immobilizing a photocatalyst using Fe_3O_4 nanoparticles can effectively increase the cyclic utilization rate and improve the photodegradation efficiency of the catalyst.[25–29] The preparation of magnetically separable visible-light-driven photocatalysts based on Fe_3O_4 is an active research field. However, to the best of our knowledge, g-C_3N_4/α-Fe_2O_3/Fe_3O_4 composites have not previously been prepared or their photo-Fenton catalytic properties investigated.

In the work presented here a novel magnetic g-C_3N_4/α-Fe_2O_3/Fe_3O_4 composite was synthesized using a simple hydrothermal method. The heterogeneous photo-Fenton activity of the g-C_3N_4/α-Fe_2O_3/Fe_3O_4 composite was investigated using the composite to degrade Orange II, a typical recalcitrant organic contaminant. The effects of the g-C_3N_4/α-Fe_2O_3 to Fe_3O_4 weight ratio, scavengers of reactive species, and the role of hydrogen peroxide (H_2O_2) on the photocatalytic activity of the composite were investigated in detail. The results demonstrated that successfully combining monodispersed Fe_3O_4 nanoparticles and g-C_3N_4/α-Fe_2O_3 enhanced light harvesting, retarded photogenerated electron–hole recombination, and significantly enhanced the photocatalytic activity of the g-C_3N_4/α-Fe_2O_3/Fe_3O_4. The magnetic recovery and reusability of the composite were also investigated, and the results indicated that the g-C_3N_4/α-Fe_2O_3/Fe_3O_4 composite will be a valuable photocatalyst that could be used to organic dye wastewater treatment.

2. Experimental

2.1. Chemical reagents and materials

Ferric chloride ($FeCl_3 \cdot 6H_2O$ 99%) and polyethylene glycol 4000 (PEG-4000) were purchased from Shanghai Chemical Reagents Company (Shanghai, China). Urea (99%) was purchased from Kermel (Tianjin, China) and $NaBH_4$ (AR) was purchased from Da mao (Tianjin, China). TCNE (98%), Orange II (99.9%, $C_{16}H_{11}N_2NaO_4S$) and sodium acetate (NaAc 99%) were provided by Acros Organics (New Jersey, USA). Ethylene glycol (EG $\geq$ 99%) was purchased from Sigma-Aldrich. Coumarin (COU 99%) was purchased from J&K Scientific Ltd. (Beijing China). All chemicals were analytical grade and used as received without further purification.

2.2. Characterization

The crystal phases of the sample were analyzed by X-ray diffraction (XRD: Rigaku Ultima IV, Japan). A scanning electron microscope (SEM, JSM-7500F, JEOL, Japan) was used to characterize the morphology of the obtained products. The composite of the sample was investigated by the energy dispersive spectroscopy (EDS) attached to the SEM. The structure and morphology of the products were examined by transmission electron microscopy (TEM: JEOL2100, Japan). Fourier transform infrared spectra (FT-IR) were measured using Spectrum One infrared spectrometer with KBr as the reference. The photoluminescence spectra (PL) of samples were measured with a fluorescence spectrophotometer (LSP920, UK) using a Xe lamp as an excitation source with optical filters. UV-vis diffuse reflectance spectroscopy was recorded with a spectrophotometer (UV-2700, shimadzu Japan). The PL spectra of hydroxyl radical ($^{\bullet}OH$) detection were measured by a fluorescence spectrophotometer (Cray Eclipse, Agilent Technologies Australia). The specific surface area and pore size distributions were measured with liquid nitrogen at 77 K using a Micromeritics ASAP 2020 instrument *via* the Brunauer–Emmett–Teller (BET) method (Quantachrome, USA). The magnetic property was measured by Physical Property Measurement System (PPMS, XL-5 Quantum Design USA) at room temperature.

2.3. Preparation of the samples

2.3.1. Synthesis of g-C_3N_4. Graphitic carbon nitride was prepared using a thermo-induced copolymerization method using urea as the precursor.[30] Urea (30 g) and tetracyanoethylene (40 mg) were mixed carefully, then the mixture was placed in a crucible with a loose cover. The crucible was placed in a muffle furnace, and the temperature was increased at 20 °C min^{-1} to 550 °C, then held for 4 h. The crucible was cooled to room temperature, then the g-C_3N_4 produced was ground to a powder to prepare it for further use.

2.3.2. Synthesis of Fe_3O_4. The Fe_3O_4 was synthesized using a solvothermal method in our previous report.[31] $FeCl_3 \cdot 6H_2O$ (0.6757 g) was dissolved in ethylene glycol (20 mL) in a sonication bath to give a yellow transparent solution. Anhydrous sodium acetate (1.6404 g) was added, and the mixture was heated until the reactants were fully dissolved, then polyethylene glycol 4000 (0.3 g) was added. The mixture was transferred to a Teflon-lined stainless steel autoclave (50 mL capacity), which was heated to 200 °C and kept at that temperature for 12 h. The autoclave was allowed to cool naturally to room temperature. The products were separated using a magnet, rinsed several times with deionized water and then ethanol, and then dried at 60 °C for 24 h.

2.3.3. Preparation of g-C_3N_4/α-Fe_2O_3/Fe_3O_4 composites. The g-C_3N_4/α-Fe_2O_3/Fe_3O_4 composites were prepared using borohydride ($NaBH_4$) reduction method and hydrothermal method. First, as-prepared Fe_3O_4 (an appropriate amount for the desired product) and g-C_3N_4 (0.3 g) were dispersed in deionized water (12.5 mL) with ultrasonication, then $FeCl_3 \cdot 9H_2O$ (0.6757 g) was dissolved in the suspension with stirring. Second, a $NaBH_4$ solution which pre-prepared by dissolving solid $NaBH_4$ (0.1892 g) in deionized water (12.5 mL) was quickly added to the suspension described above, and the mixture was vigorously stirred for 1 h. In this process, the ferric ion (Fe^{3+}) was reduced to zero-valent iron (Fe^0).[32] Third, the above mixture was then transferred to a Teflon-lined stainless steel autoclave

(50 mL capacity), which was heated to 120 °C for 12 h to allow the Fe^0 oxidized to α-Fe_2O_3,[33] then the desired g-C_3N_4/α-Fe_2O_3/Fe_3O_4 composite was formed. Last, the suspension produced was washed several times with deionized water and ethanol, then dried at 60 °C. Composite samples with different Fe_3O_4 mass fractions were produced, and they are later labeled g-C_3N_4/α-Fe_2O_3/Fe_3O_4 (x), where x is the Fe_3O_4 mass percent in the g-C_3N_4/α-Fe_2O_3/Fe_3O_4 composite. Samples with Fe_3O_4 mass percentages of 10%, 20%, 30%, 40%, and 45% were prepared using the procedure described above. A schematic diagram of the growth process of the g-C_3N_4/α-Fe_2O_3/Fe_3O_4 composites is shown in Fig. 1.

2.4. Photodegradation of Orange II

The photocatalytic efficiencies of the samples that were prepared were evaluated using the samples to degrade Orange II in the presence of H_2O_2 and irradiated with visible light produced using a Xe light (500 W) with a 420 nm cut-off filter. For a degradation experiment, a 50 mg L^{-1} (the initial concentration, C_0) stock solution (100 mL) of Orange II was placed in a glass beaker, then the catalyst being tested was added and the mixture was put in a dark place and constantly stirred using a magnetic stirrer for 30 min to allow absorption–desorption equilibrium to be reached. H_2O_2 (0.1 mL) was then added and the mixture was immediately irradiated with visible light. All the tests were performed at a constant temperature of 25 ± 0.2 °C, achieved using a water bath. A 3.0 mL aliquot of the solution was removed at each of a series of specified times, and absorbance at 484 nm was measured using a UV-visible spectrophotometer.

2.5. Measurement of ˙OH

The formation of ˙OH was detected by the PL technique using COU as a probe molecule. Experimental procedures were as follows: 0.1 g of g-C_3N_4/α-Fe_2O_3/Fe_3O_4 composites was dispersed in 100 mL of 1 × 10^{-3} M COU aqueous solution in a glass beaker, then the solution was constantly stirred using a magnetic stirrer for 30 min to allow absorption–desorption equilibrium to be reached. H_2O_2 (0.1 mL) was then added and the mixture was immediately irradiated with visible light using a Xe light (500 W) with a 420 nm cut-off filter. All the tests were performed at a constant temperature of 25 ± 0.2 °C, achieved using a water bath. A 3.0 mL aliquot of the solution was removed at each of 15 min, and the reaction solution was filtrated to measure the PL intensity at 456 nm by an Agilent Technologies Cary Eclipse Fluorescence Spectrophotometer. The excitation wavelength was 332 nm, the scanning speed was 120 nm min^{-1}. The width of excitation and emission slit was set to be both 5 nm.

Fig. 1 The schematic diagram for growth process of the g-C_3N_4/α-Fe_2O_3/Fe_3O_4 composites.

3. Results and discussion

The X-ray diffraction patterns of the g-C_3N_4, α-Fe_2O_3, Fe_3O_4, and g-C_3N_4/α-Fe_2O_3 materials and the g-C_3N_4/α-Fe_2O_3/Fe_3O_4 composites with different Fe_3O_4 contents are shown in Fig. 2a. The g-C_3N_4 gave a pronounced peak at 27.5° indexed as a (002) diffraction plane corresponding to the characteristic interlayer stacking peak of a conjugated aromatic system (JCPDS files no. 87-1526).[34] The positions and relative intensities of all the diffraction peaks for the Fe_3O_4 sample matched the data for pure face-centered cubic Fe_3O_4, and the diffraction peaks in the range 30.6–63.2° were indexed as (220), (311), (400), (422), (511), and (440) reflections (JCPDS files no. 19-0629).[35] Diffraction peaks were found for α-Fe_2O_3 at 24.2°, 33.3°, 35.7°, 40.9°, and 49.5°, and these were indexed as (012), (104), (110), (113), and (024) planes of α-Fe_2O_3, respectively (JCPDS files no. 33-0664).[16] The g-C_3N_4/α-Fe_2O_3/Fe_3O_4 composite X-ray diffraction patterns contained the diffraction peaks for g-C_3N_4, α-Fe_2O_3, and Fe_3O_4, and the intensity of the Fe_3O_4 peak increased as the Fe_3O_4 weight percent increased. This suggested that the desired g-C_3N_4/α-Fe_2O_3/Fe_3O_4 composites were successfully prepared using the hydrothermal method.

Fourier-transform infrared spectra were acquired to characterize the structural properties of the samples, and the results are shown in Fig. 2b. The g-C_3N_4 sample gave a broad band at 3400 cm^{-1} indicative of N–H stretching vibrations and a band in the range 1214–1634 cm^{-1} corresponding to heterocycle C–N and C=N stretching vibrations.[36] A breathing mode at 806 cm^{-1} was related to typical *s*-triazine unit bending vibrations.[37] The composites containing Fe_3O_4 and α-Fe_2O_3 had characteristic peaks at 470 and 560 cm^{-1} attributed to Fe–O stretching.[38,39] It can be seen that the main characteristic peaks of g-C_3N_4, Fe_3O_4, and α-Fe_2O_3 were found in the g-C_3N_4/α-Fe_2O_3/Fe_3O_4 composite spectra, further demonstrating that α-Fe_2O_3 and Fe_3O_4 had been deposited on the surfaces of the g-C_3N_4 sheets.

The morphologies of the samples and the ways in which the samples formed were investigated using scanning electron microscopy and transmission electron microscopy. Scanning electron microscopy images for g-C_3N_4, Fe_3O_4, and g-C_3N_4/α-Fe_2O_3/Fe_3O_4 (30%) are shown in Fig. 3a–c, respectively. The pristine g-C_3N_4 sample had a sheet-like structure. The Fe_3O_4 nanoparticles were nearly spherical. In contrast, the g-C_3N_4/α-Fe_2O_3/Fe_3O_4 composite produced using the 12 h hydrothermal reaction process was irregular and rough in shape because of the Fe_3O_4 and α-Fe_2O_3 deposited on the g-C_3N_4 surfaces. It can be seen from the transmission electron microscopy images

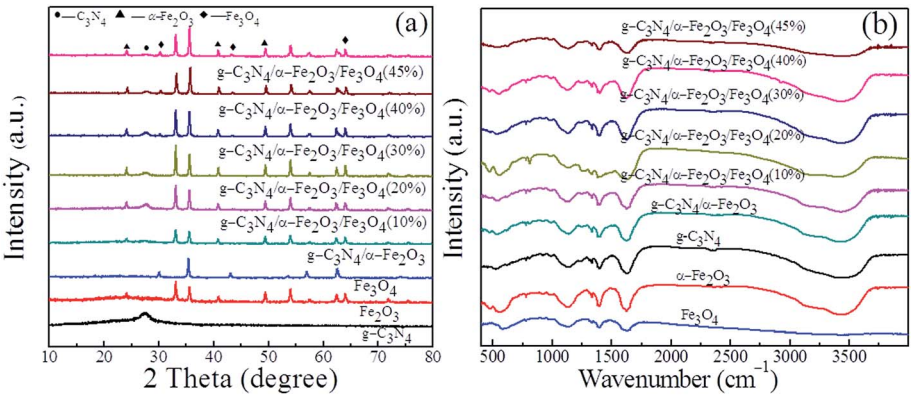

Fig. 2 (a) XRD patterns and (b) FT-IR spectra of g-C_3N_4, Fe_3O_4, α-Fe_2O_3 and g-C_3N_4/α-Fe_2O_3/Fe_3O_4 samples.

shown in Fig. 3d and e that the pristine g-C_3N_4 had typical two-dimensional sheet-like nanosheets and that the Fe_3O_4 were very dispersible. It can clearly be seen from the g-C_3N_4/α-Fe_2O_3/Fe_3O_4 transmission electron microscopy image shown in Fig. 3f that Fe_3O_4 and α-Fe_2O_3 particles were uniformly distributed over the g-C_3N_4 sheet surfaces and a sandwich-like structure was formed. This unique architecture can greatly promote separation efficiency of electron–hole pairs. High resolution transmission electron microscopy (HRTEM) image of g-C_3N_4/α-Fe_2O_3/Fe_3O_4 is shown in Fig. 3g. It can be noted that there are two different lattice fringes on the surface of g-C_3N_4, the lattice fringe of 0.271 nm and 0.253 nm in the observed nanocrystallites agrees well with the (104) lattice planes of α-Fe_2O_3 and the (311) lattice planes of Fe_3O_4, respectively, which indicates the existence of the heterojunction structure between g-C_3N_4, α-Fe_2O_3 and Fe_3O_4.[40,41]

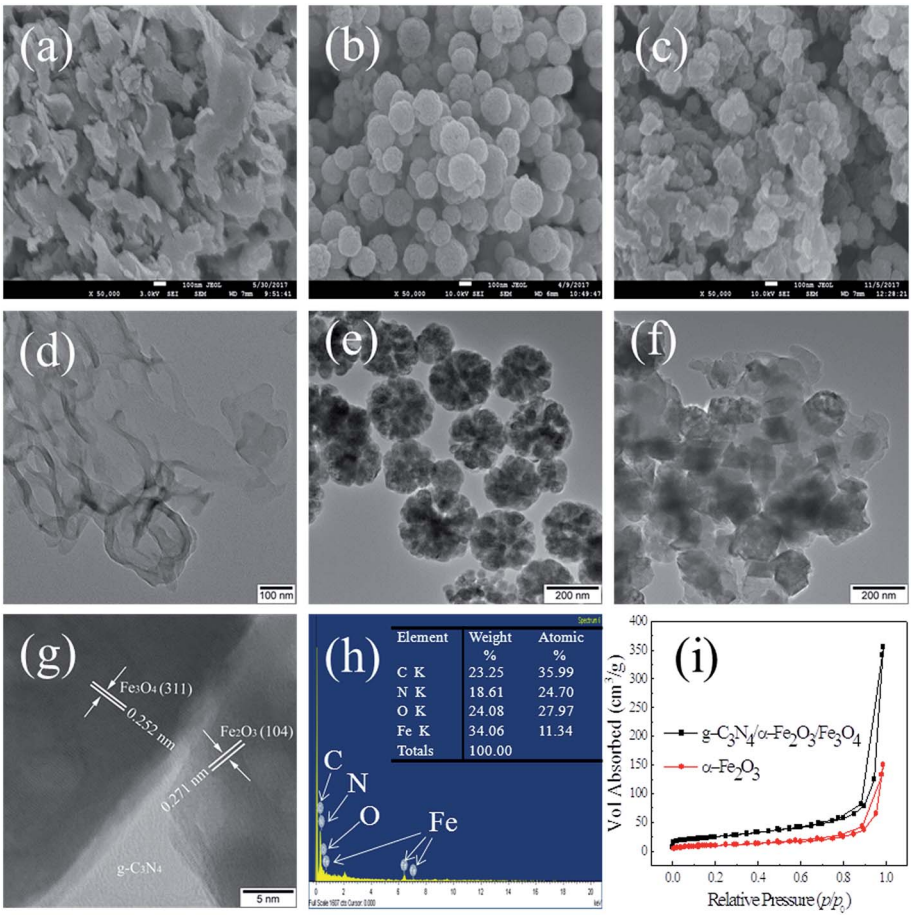

Fig. 3 SEM (a–c), TEM (d–f), HRTEM (g), EDX (h), and N_2 adsorption–desorption isotherm (i) of the samples.

Energy dispersive spectroscopy was performed to determine the elemental composition of the g-C_3N_4/α-Fe_2O_3/Fe_3O_4 (30%) sample, and the results are shown in Fig. 3d. The peaks were ascribed to the elements C, N, O, and Fe and agreed with the X-ray diffraction patterns, further confirming the presence of g-C_3N_4, Fe_3O_4, and α-Fe_2O_3 particles in the composite. The specific surface areas of the α-Fe_2O_3 and the g-C_3N_4/α-Fe_2O_3/Fe_3O_4 (30%) composite were determined by acquiring N_2 adsorption/desorption isotherms (Fig. 2h). Both samples gave type IV adsorption–desorption isotherms according to the Brunauer–Deming–Deming–Teller classification. Type IV adsorption–desorption isotherms are typical of materials with mesoporous domains. The BET surface area of g-C_3N_4/α-Fe_2O_3/Fe_3O_4 (30%) was 88.37 $m^2\ g^{-1}$, which was much higher than the surface area of α-Fe_2O_3 (38.54 $m^2\ g^{-1}$). Importantly, the pore volume was also higher for g-C_3N_4/α-Fe_2O_3/Fe_3O_4 (30%), at 0.55 $cm^3\ g^{-1}$, than for α-Fe_2O_3 (0.23 $cm^3\ g^{-1}$). The high pore volume of g-C_3N_4/α-Fe_2O_3/Fe_3O_4 (30%) would have facilitated charge separation in the composite system and made the composite suitable for heterogeneous photo-Fenton applications.[24]

It is well known that enhancing absorption in the visible-light region improves the activity of a photocatalyst. The UV-vis diffuse reflection spectra of α-Fe_2O_3, g-C_3N_4/α-Fe_2O_3, and g-C_3N_4/α-Fe_2O_3/Fe_3O_4 with different Fe_3O_4 weight percentages were acquired and are shown in Fig. 4a. α-Fe_2O_3 had an absorption threshold at 657 nm associated with a band gap energy of 1.9 eV, which agreed with the previously reported band gap energy.[42] g-C_3N_4/α-Fe_2O_3 had an absorption threshold at 617 nm associated with a band gap energy of 2.01 eV, which was lower than the band gap energy of pure g-C_3N_4 (~2.7 eV). The g-C_3N_4/α-Fe_2O_3/Fe_3O_4 (10%), g-C_3N_4/α-Fe_2O_3/Fe_3O_4 (30%), and g-C_3N_4/α-Fe_2O_3/Fe_3O_4 (45%) absorption thresholds were at 627, 661, and 669 nm, respectively, and the band gap energies were 1.98, 1.88, and 1.85 eV, respectively. These results indicate that the g-C_3N_4/α-Fe_2O_3/Fe_3O_4 composite absorption edge shifted to a longer wavelength and the ability to absorb visible light improved as the Fe_3O_4 to g-C_3N_4/α-Fe_2O_3 weight ratio increased. The increase in visible light absorption may have been caused by heterogeneous structures forming. The results imply that the response of the photocatalyst to visible light was improved by loading Fe_3O_4 and α-Fe_2O_3 onto the g-C_3N_4 sheets, which may have increased the photocatalytic activity by allowing more photogenerated charge carriers to be formed.

The migration, transfer, and recombination processes for the photogenerated electron–hole pairs in the samples were investigated by acquiring room temperature PL spectra of α-Fe_2O_3, g-C_3N_4/α-Fe_2O_3, and the g-C_3N_4/α-Fe_2O_3/Fe_3O_4 composites. The spectra are shown in Fig. 4b. No obvious α-Fe_2O_3 emission peak was found because the α-Fe_2O_3 peak intensity was much weaker than the g-C_3N_4/α-Fe_2O_3 and g-C_3N_4/α-Fe_2O_3/Fe_3O_4 composite peak intensities.[21] The main g-C_3N_4/α-Fe_2O_3 and g-C_3N_4/α-Fe_2O_3/Fe_3O_4 composite emission bands were centered on 480 nm, and the g-C_3N_4/α-Fe_2O_3/Fe_3O_4 composite emission peaks were much weaker than the pure g-C_3N_4/α-Fe_2O_3 emission peak, indicating that the recombination of photogenerated electron–hole pairs was efficiently hampered. The emission peak became weaker as the amount of Fe_3O_4 present increased, meaning the lifetimes of the photogenerated charge carriers would have increased as the amount of Fe_3O_4 present increased.

The photo-Fenton photocatalytic activities of α-Fe_2O_3, g-C_3N_4/α-Fe_2O_3, and g-C_3N_4/α-Fe_2O_3/Fe_3O_4 composites were determined using the catalysts to decompose Orange II when irradiated with visible light (λ > 420 nm). As shown in Fig. 5a, Orange II was degraded by each sample, and the photocatalytic activities of the composites were closely related to the compositions of the composites. All the g-C_3N_4/α-Fe_2O_3/Fe_3O_4 samples had stronger photocatalytic activities than did α-Fe_2O_3 and g-C_3N_4/α-Fe_2O_3. The enhanced photocatalytic activities of the composites could have been caused by the composites having higher surface areas, higher visible-light absorption capacities, and higher electron–hole separation efficiencies.

The experimental data were analyzed to investigate the Orange II degradation kinetics, and it was found that a pseudo-first-order model fitted the data. The formula for the pseudo-first-order model is

$$\ln(c_0/c) = kt,$$

where c_0 is the initial Orange II concentration in the aqueous solution, c is the actual Orange II concentration at the specified reaction time, k is the degradation rate constant, and t is the reaction time. The rate constants k for the different samples are

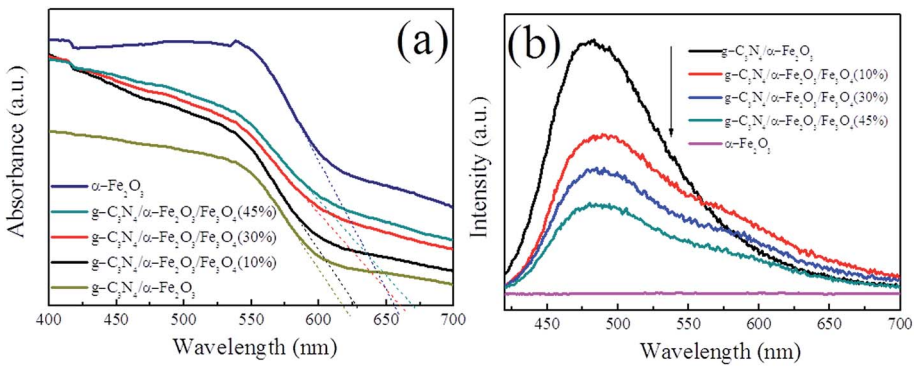

Fig. 4 UV-vis DRS (a) and PL spectra (b) of α-Fe_2O_3, g-C_3N_4/α-Fe_2O_3, and g-C_3N_4/α-Fe_2O_3/Fe_3O_4 samples.

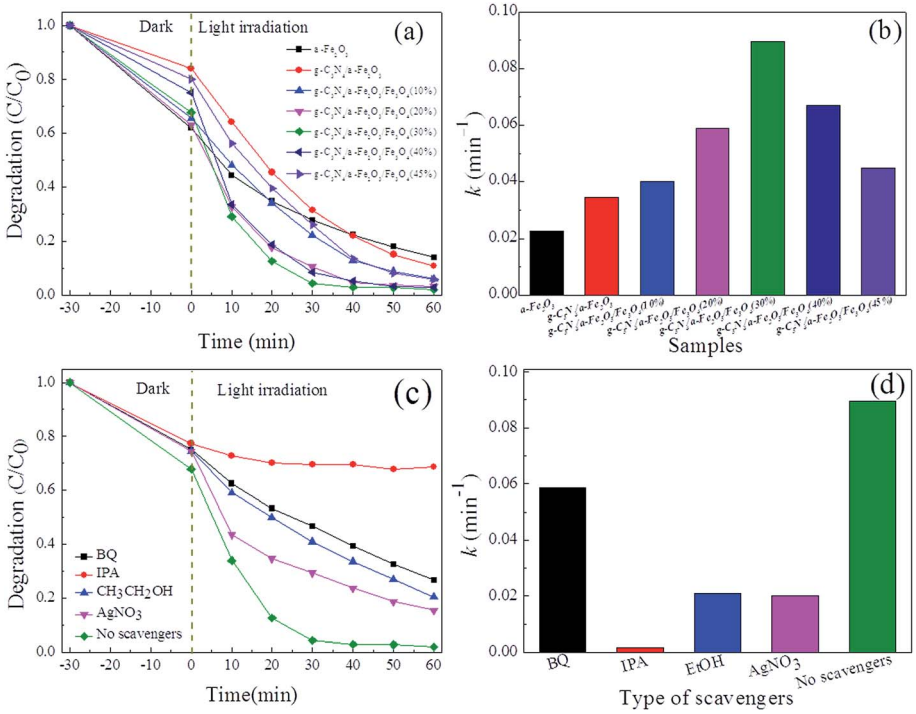

Fig. 5 (a) Degradation rate and (b) kinetic constant of all samples, (c) degradation rate and (d) kinetic constant of g-C_3N_4/α-Fe_2O_3/Fe_3O_4 (30%) samples with different scavengers.

shown in Fig. 5b. It is worth noting that the photocatalytic activities of the samples first increased and then decreased as the amount of Fe_3O_4 present increased. The g-C_3N_4/α-Fe_2O_3/Fe_3O_4 composite with a Fe_3O_4 mass content of 30% had the highest rate constant, 0.091 min^{-1}, which was almost 4.01 times higher than the rate constant for α-Fe_2O_3 and 2.65 times higher than the rate constant for g-C_3N_4/α-Fe_2O_3. This may have been because combining a little Fe_3O_4 with α-Fe_2O_3 and g-C_3N_4 could allow heterojunctions to form, giving the composite a lower rate of electron–hole pair recombination. This would have meant that more h^+ and e^- would have been generated to participate in the degradation process, enhancing the photocatalytic activity.[43] However, increasing the amount of Fe_3O_4 present further would have allowed some Fe_3O_4 to act as a recombination center for photoinduced electrons and holes,[34] and may have caused the active sites on the g-C_3N_4 surfaces to be covered, decreasing the photocatalytic activity of the composite. It is therefore very important that the most appropriate degree of doping is achieved to improve photocatalytic activity.

The reactive species trapping experiments were performed to evaluate role of the active species in the photocatalytic process. 1,4-Benzoquinone (BQ), isopropanol (IPA), ethanol (EtOH), and silver nitrate ($AgNO_3$) were used to capture superoxide radicals ($^{\bullet}O_2^-$), hydroxyl radicals ($^{\bullet}OH$), holes (h^+), and electrons (e^-), respectively.[44,45] The results of degradation rate and kinetic constant of g-C_3N_4/α-Fe_2O_3/Fe_3O_4 (30%) samples with different scavengers are shown in Fig. 5c and d. It can be seen that using IPA as a radical scavenger markedly decreased the degradation rate, indicating that $^{\bullet}OH$ radicals were involved in the photocatalytic process. Likewise, using EtOH, BQ, and $AgNO_3$ decreased the degradation rate to some extent, indicating that $^{\bullet}O_2^-$, h^+, and e^- also played roles in the photocatalytic process.

To further detect the formation of $^{\bullet}OH$ in our visible-light-Fenton system, the PL technique was performed using COU as a probe molecule according to the published literatures.[46,47] Because of COU can readily react with $^{\bullet}OH$ to produce highly fluorescent product, 7-hydroxycoumarin (7HC), we can detect the formation of $^{\bullet}OH$ by the PL spectra of 7HC in an aqueous solution containing g-C_3N_4/α-Fe_2O_3/Fe_3O_4 composite, COU and H_2O_2 under visible light irradiation. As shown in Fig. 6a, a gradual increase in the PL intensity at about 456 nm was observed with increasing irradiation time, which indicated that fluorescent product 7HC was formed during visible-light-Fenton process due to the specific reaction between $^{\bullet}OH$ and COU. Thus, it could be inferred that the $^{\bullet}OH$ is producing at the g-C_3N_4/α-Fe_2O_3/Fe_3O_4 composites surface, which is consistent with the results of reactive species trapping experiments.

The results described above led us to propose the catalytic mechanism for the g-C_3N_4/α-Fe_2O_3/Fe_3O_4 composite shown in Fig. 6b. There are five main possible aspects to the Orange II catalytic degradation process. (i) Both α-Fe_2O_3 and g-C_3N_4 can efficiently absorb visible light and form photogenerated electron–hole pairs (eqn (1)) because the g-C_3N_4 and α-Fe_2O_3 band gap energies are about 2.70 and 1.90 eV, respectively. (ii) The Fe(III) on the α-Fe_2O_3 surfaces may be reduced to Fe(II) by excited electrons, then Fe(II) could react with H_2O_2 to form the Fenton system, generating $^{\bullet}HO$ radicals (eqn (3)). (iii) The g-C_3N_4 conduction band bottom level is more negative than the O_2/$^{\bullet}O_2^-$ redox potential (−0.16 eV),[48] so the photogenerated

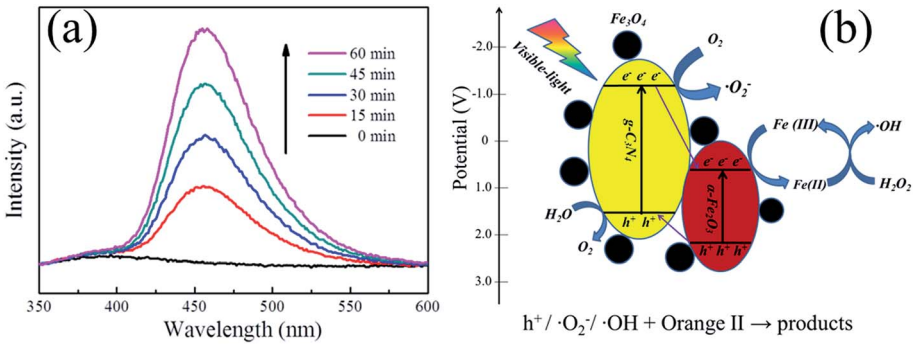

Fig. 6 (a) PL spectra of COU solution with g-C_3N_4/α-Fe_2O_3/Fe_3O_4 composite in the presence of H_2O_2 under visible light irradiation. (b) Possible mechanism for the enhanced activity of g-C_3N_4/α-Fe_2O_3/Fe_3O_4 composite.

electrons in the g-C_3N_4 conduction band could react with O_2 on the photocatalyst surfaces to form $^{\bullet}O_2^-$ radicals (eqn (4)). (iv) The presence of heterojunctions between α-Fe_2O_3 and g-C_3N_4 may allow the holes generated in the α-Fe_2O_3 valence band to be transferred to the g-C_3N_4 valence band. The photogenerated holes could react with H_2O to produce O_2 (eqn (5)), and the O_2 generated could react with electrons to generate $^{\bullet}O_2^-$. Likewise, the electrons generated in the g-C_3N_4 conduction band could be transferred to the α-Fe_2O_3 conduction band, reducing more Fe(III) to Fe(II) on the α-Fe_2O_3 surfaces, directly contributing to the production of $^{\bullet}$HO radicals.

The g-C_3N_4/α-Fe_2O_3/Fe_3O_4 catalyst also had a high surface area to which Orange II could adsorb, benefiting the degradation process. It is worth noting that the high conductivity of Fe_3O_4 will mean that some Fe_3O_4 between the α-Fe_2O_3 and g-C_3N_4 nanosheet interfaces could act as a medium for the transmission of electrons and holes between g-C_3N_4 and α-Fe_2O_3, strongly decreasing the probability that photogenerated electron–hole pairs in the g-C_3N_4/α-Fe_2O_3/Fe_3O_4 composite system will recombine. This will cause more electrons and holes to form active species that could be involved in the photodegradation of Orange II. This photo-Fenton system works through $^{\bullet}$OH, $^{\bullet}O_2^-$, and holes that all acting as reactive species (eqn (6)), significantly increasing the photocatalytic activity relative to a traditional Fenton system.

$$\text{g-}C_3N_4/\alpha\text{-}Fe_2O_3/Fe_3O_4 + h\nu \rightarrow e^- + h^+ \quad (1)$$

$$Fe(III) + e^- \rightarrow Fe(II) \quad (2)$$

$$H_2O_2 + Fe(II) \rightarrow Fe(III) + {}^{\bullet}OH + OH^- \quad (3)$$

$$O_2 + e^- \rightarrow {}^{\bullet}O_2^- \quad (4)$$

$$h^+ + H_2O \rightarrow O_2 \quad (5)$$

$$h^+/{}^{\bullet}O_2^-/{}^{\bullet}OH + \text{Orange II} \rightarrow \text{products} \quad (6)$$

The magnetic properties of Fe_2O_3, Fe_3O_4 and the g-C_3N_4/α-Fe_2O_3/Fe_3O_4 composites were measured at room temperature, and the results are shown in Fig. 7a. The α-Fe_2O_3 magnetization curve showed that α-Fe_2O_3 was almost non-magnetic. Saturation magnetization for Fe_3O_4 and g-C_3N_4/α-Fe_2O_3/Fe_3O_4 was found at about 83.58 and 17.98 emu g^{-1}, respectively. The saturated magnetization was lower for g-C_3N_4/α-Fe_2O_3/Fe_3O_4 than for the Fe_3O_4 nanoparticles because of the presence of nonmagnetic g-C_3N_4 and α-Fe_2O_3. Separation of the magnetic photocatalyst from a treated solution using a magnet is shown in the inset in Fig. 7a. We concluded that the nanocomposite was magnetic enough to allow the composite to be magnetically separated from a treated solution.

The reusability of a photocatalyst is an important parameter from the economic viewpoint. Recycling tests were conducted to

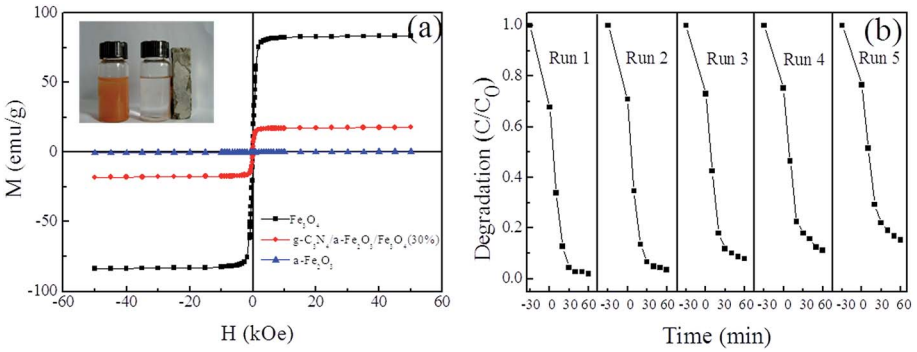

Fig. 7 (a) Magnetization curves for the α-Fe_2O_3, Fe_3O_4 nanoparticles and g-C_3N_4/α-Fe_2O_3/Fe_3O_4 (30%) composite. Inset of the figure shows separation of the composite from the treated solution using a magnet. (b) Reusability of the nanocomposite after five successive runs.

investigate the stability of g-C_3N_4/α-Fe_2O_3/Fe_3O_4, and the results are shown in Fig. 7b. More than 85% of the original photocatalytic activity of g-C_3N_4/α-Fe_2O_3/Fe_3O_4 (30%) was retained after five successive experimental runs using the same experimental conditions. The photocatalytic activity may have decreased with repeated use because of photocorrosion of the nanocomposite. These results indicated that the g-C_3N_4/α-Fe_2O_3/Fe_3O_4 catalyst is quite stable and could be reused.

4. Conclusions

Magnetic heterogeneous g-C_3N_4/α-Fe_2O_3/Fe_3O_4 composites with different Fe_3O_4 mass percentages were successfully fabricated *via* a facile hydrothermal synthesis route. Combining the Fenton and photocatalytic processes in one reaction system gave the composite excellent catalytic activity. Of the samples that were prepared, g-C_3N_4/α-Fe_2O_3/Fe_3O_4 (30%) had the best catalytic activity. The enhanced photocatalytic activities could be ascribed to increases in the surface area, visible light absorption capacity, and electron–hole separation efficiency, leading to more h^+ and e^- being generated to participate in the degradation process. A possible catalytic mechanism for the g-C_3N_4/α-Fe_2O_3/Fe_3O_4 composite was proposed. This photo-Fenton system works through $^{\bullet}OH$, $^{\bullet}O_2^-$, and holes that all acting as reactive species, significantly increasing the photocatalytic activity relative to a traditional Fenton system. The g-C_3N_4/α-Fe_2O_3/Fe_3O_4 catalyst could be reused and was magnetic enough to be easily separated from a treated solution. The simply prepared magnetic heterogeneous composite was found to be an effective visible-light-driven photo-Fenton catalyst that may be useful in environmental applications.

Conflicts of interest

The authors declare no competing financial interest.

Acknowledgements

This work was supported by the National Science Foundation of China (Grant No. 61434002), the Special Funds of Sanjin Scholars Program.

References

1 H. Lin, H. Zhang, X. Wang, L. Wang and J. Wu, *Sep. Purif. Technol.*, 2014, **122**, 533–540.
2 M. A. Oturan and J.-J. Aaron, *Crit. Rev. Environ. Sci. Technol.*, 2014, **44**, 2577–2641.
3 L. Clarizia, D. Russo, I. Di Somma, R. Marotta and R. Andreozzi, *Appl. Catal., B*, 2017, **209**, 358–371.
4 S. Rahim Pouran, A. R. Abdul Aziz and W. M. A. Wan Daud, *J. Ind. Eng. Chem.*, 2015, **21**, 53–69.
5 M. Sayed, J. A. Khan, L. A. Shah, N. S. Shah, F. Shah, H. M. Khan, P. Zhang and H. Arandiyan, *J. Phys. Chem. C*, 2017, **122**, 406–421.
6 M. Sayed, L. A. Shah, J. A. Khan, N. S. Shah, J. Nisar, H. M. Khan, P. Zhang and A. R. Khan, *J. Phys. Chem. A*, 2016, **120**, 9916–9931.
7 A. M. Khan, A. Mehmood, M. Sayed, M. F. Nazar, B. Ismail, R. A. Khan, H. Ullah, H. M. Abdur Rehman, A. Y. Khan and A. R. Khan, *J. Mol. Liq.*, 2017, **236**, 395–403.
8 H. Li, Y. Li, L. Xiang, Q. Huang, J. Qiu, H. Zhang, M. V. Sivaiah, F. Baron, J. Barrault, S. Petit and S. Valange, *J. Hazard. Mater.*, 2015, **287**, 32–41.
9 J. M. Monteagudo, A. Durán and C. López-Almodóvar, *Appl. Catal., B*, 2008, **83**, 46–55.
10 A. Mirzaei, Z. Chen, F. Haghighat and L. Yerushalmi, *Chemosphere*, 2017, **174**, 665–688.
11 X. Zhang, Y. Ding, H. Tang, X. Han, L. Zhu and N. Wang, *Chem. Eng. J.*, 2014, **236**, 251–262.
12 J. A. Khan, X. He, N. S. Shah, M. Sayed, H. M. Khan and D. D. Dionysiou, *Chem. Eng. J.*, 2017, **325**, 485–494.
13 D. B. Jiang, X. Liu, X. Xu and Y. X. Zhang, *J. Phys. Chem. Solids*, 2018, **112**, 209–215.
14 L. Zhou, J. Lei, L. Wang, Y. Liu and J. Zhang, *Appl. Catal., B*, 2017, DOI: 10.1016/j.apcatb.2017.08.039.
15 J. Zhang, T. Yao, C. Guan, N. Zhang, H. Zhang, X. Zhang and J. Wu, *J. Colloid Interface Sci.*, 2017, **505**, 130–138.
16 Q. Tian, W. Wu, L. Sun, S. Yang, M. Lei, J. Zhou, Y. Liu, X. Xiao, F. Ren, C. Jiang and V. A. L. Roy, *ACS Appl. Mater. Interfaces*, 2014, **6**, 13088–13097.
17 L. Qin, M. Liu, Y. Wu, Z. Xu, X. Guo and G. Zhang, *Appl. Catal., B*, 2016, **194**, 50–60.
18 B. Liu, L. Tian, R. Wang, J. Yang, R. Guan and X. Chen, *Appl. Surf. Sci.*, 2017, **422**, 607–615.
19 S. Guo, G. Zhang, Y. Guo and J. C. Yu, *Carbon*, 2013, **60**, 437–444.
20 D. Bi and Y. Xu, *Langmuir*, 2011, **27**, 9359–9366.
21 D. Xiao, K. Dai, Y. Qu, Y. Yin and H. Chen, *Appl. Surf. Sci.*, 2015, **358**, 181–187.
22 S. Hu, R. Jin, G. Lu, D. Liu and J. Gui, *RSC Adv.*, 2014, **4**, 24863.
23 A. Akhundi and A. Habibi-Yangjeh, *Ceram. Int.*, 2015, **41**, 5634–5643.
24 S. Kumar, S. T, B. Kumar, A. Baruah and V. Shanker, *J. Phys. Chem. C*, 2013, **117**, 26135–26143.
25 D. Zhu, S. Liu, M. Chen, J. Zhang and X. Wang, *Colloids Surf., A*, 2018, **537**, 372–382.
26 D. Zhang, S. Cui and J. Yang, *J. Alloys Compd.*, 2017, **708**, 1141–1149.
27 J. Wang, Y. Chen, G. Liu and Y. Cao, *Composites, Part B*, 2017, **114**, 211–222.
28 R. Nagarjuna, S. Challagulla, R. Ganesan and S. Roy, *Chem. Eng. J.*, 2017, **308**, 59–66.
29 S. Hu, W. Ouyang, L. Guo, Z. Lin, X. Jiang, B. Qiu and G. Chen, *Biosens. Bioelectron.*, 2017, **92**, 718–723.
30 M. Zhang and X. Wang, *Energy Environ. Sci.*, 2014, **7**, 1902.
31 N. Gao, H. Wu, Y. Chang, X. Guo, L. Zhang, L. Du and Y. Fu, *Spectrochim. Acta, Part A*, 2015, **134**, 10–16.
32 Y.-P. Sun, X.-q. Li, J. Cao, W.-x. Zhang and H. P. Wang, *Adv. Colloid Interface Sci.*, 2006, **120**, 47–56.

33 C. Cai, Z. Zhang, J. Liu, N. Shan, H. Zhang and D. D. Dionysiou, *Appl. Catal., B*, 2016, **182**, 456–468.
34 X. Zhou, B. Jin, R. Chen, F. Peng and Y. Fang, *Mater. Res. Bull.*, 2013, **48**, 1447–1452.
35 X. Li, X. Huang, D. Liu, X. Wang, S. Song, L. Zhou and H. Zhang, *J. Phys. Chem. C*, 2011, **115**, 21567–21573.
36 E. S. Baeissa, *Frontiers in Nanoscience and Nanotechnology*, 2016, **2**, 100–106.
37 M. Mousavi and A. Habibi-Yangjeh, *J. Colloid Interface Sci.*, 2016, **465**, 83–92.
38 X. Zhang, S. Lin, Z. Chen, M. Megharaj and R. Naidu, *Water Res.*, 2011, **45**, 3481–3488.
39 T. Wang, X. Jin, Z. Chen, M. Megharaj and R. Naidu, *Sci. Total Environ.*, 2014, **466–467**, 210–213.
40 B. Jia, L. Gao and J. Sun, *J. Am. Ceram. Soc.*, 2007, **90**, 1315–1318.
41 P. Liu, Q. Xu, D. Gao, S. Shi and B. Xia, *Journal of Advances in Nanomaterials*, 2017, DOI: 10.22606/jan.2017.21002.
42 Y. Cui, J. Briscoe, Y. Wang, N. V. Tarakina and S. Dunn, *ACS Appl. Mater. Interfaces*, 2017, **9**, 24518–24526.
43 S. Chi, C. Ji, S. Sun, H. Jiang, R. Qu and C. Sun, *Ind. Eng. Chem. Res.*, 2016, **55**, 12060–12067.
44 E. Cheng, S. Zhou, M. Li and Z. Li, *Appl. Surf. Sci.*, 2017, **410**, 383–392.
45 W. J. Kim, E. Jang and T. J. Park, *Appl. Surf. Sci.*, 2017, **419**, 159–164.
46 K.-i. Ishibashi, A. Fujishima, T. Watanabe and K. Hashimoto, *Electrochem. Commun.*, 2000, **2**, 207–210.
47 Q. Xiang, J. Yu and P. K. Wong, *J. Colloid Interface Sci.*, 2011, **357**, 163–167.
48 F. Dong, L. Wu, Y. Sun, M. Fu, Z. Wu and S. C. Lee, *J. Mater. Chem.*, 2011, **21**, 15171–15174.